Atmospheric
Measurement
Techniques
Open Access
Discussions

Development and characterisation of a state-of-the-art GOME-2 formaldehyde air-mass factor algorithm

W. Hewson[1], M. P. Barkley[1], G. Gonzalez Abad[2], H. Bösch[1], T. Kurosu[3], and R. Spurr[4]

[1]EOS Group, Department of Physics and Astronomy, University of Leicester, Leicester, UK
[2]Atomic and Molecular Physics Division, Harvard-Smithsonian Center for Astrophysics, Cambridge, Massachusetts, USA
[3]NASA Jet Propulsion Laboratory, Pasadena, California, USA
[4]RT Solutions Inc, Cambridge, Massachusetts, USA

Correspondence to: M. P. Barkley (mpb14@le.ac.uk)

Discussion Paper | Discussion Paper | Discussion Paper | Discussion Paper

AMTD

8, 1109–1150, 2015

GOME-2 airmass factors

W. Hewson et al.

Title Page

Abstract | Introduction

Conclusions | References

Tables | Figures

◄ | ►

◄ | ►

Back | Close

Full Screen / Esc

Printer-friendly Version

Interactive Discussion

Abstract

Space-borne observations of formaldehyde (HCHO) are frequently used to derive surface emissions of isoprene, an important biogenic volatile organic compound. The conversion of retrieved HCHO slant column concentrations from satellite line of sight measurements to vertical columns is determined through application of an air mass factor (AMF), accounting for instrument viewing geometry, radiative transfer, and vertical profile of the absorber in the atmosphere. This step in the trace gas retrieval is subject to large errors. This work presents the AMF algorithm in use at the University of Leicester (UoL), which introduces scene specific variables into a per-observation full radiative transfer AMF calculation, including increasing spatial resolution of key environmental parameter databases, input variable area weighting, instrument specific scattering weight calculation, and inclusion of an ozone vertical profile climatology. Application of these updates to HCHO slant columns from the GOME-2 instrument is shown to typically adjust the AMF by ±10 %, compared to a reference algorithm without these advanced parameterisations. Furthermore, the new UoL algorithm also incorporates a full radiative transfer error calculation for each scene to help characterise AMF uncertainties. Global median AMF errors are typically 50–60 %, and are dominated by uncertainties in the HCHO profile shape and its corresponding seasonal variation.

1 Introduction

Formaldehyde (HCHO) is produced in the atmosphere from the oxidation of a wide range of volatile organic compounds (VOCs), emitted from human activities, vegetation and biomass burning (Stavrakou et al., 2008). Direct HCHO emissions from vegetation and industry are additional minor sources. The main sinks of HCHO are photolysis and reaction with the hydroxyl radical (OH), which give it a short atmospheric lifetime of only a few hours, thus making it an important tracer of localised active photochemistry and a useful proxy for determining underlying surface VOC emissions. In particular, there

has been widespread use of satellite measurements of HCHO integrated columns to constrain the emissions of isoprene, the dominant biogenic VOC (BVOC) emitted from terrestrial vegetation and a high HCHO yield precursor, at both regional and global scales (e.g., Palmer et al., 2006; Fu et al., 2007; Millet et al., 2006, 2008; Curci et al.,

5   2010; Marais et al., 2012; Barkley et al., 2008, 2013; Stavrakou et al., 2009a, b). However, reducing uncertainties associated with inferred (or top-down) emission estimates depends critically on the accuracy of the retrieved HCHO column observations (Barkley et al., 2013).

     Tropospheric vertical HCHO columns have been retrieved by a number of groups

10   from solar backscatter instruments such as GOME (Chance et al., 2000; Wittrock et al., 2000, 2006; De Smedt et al., 2008), SCIAMACHY (De Smedt et al., 2008), OMI (Kurosu et al., 2004; González Abad et al., 2014), and GOME-2 (De Smedt et al., 2008; Hewson et al., 2013). This process typically involves three stages. First, HCHO slant columns along the instrument line-of-sight are obtained via the spectral fitting of

15   trace gas absorption cross-sections to observed UV radiance measurements (typically in the wavelength range $\sim$ 325–360 nm). Second, observed HCHO column residual biases (e.g., due to ozone interference) over the remote Pacific Ocean are then removed using a standard reference sector correction (e.g., De Smedt et al., 2008, 2012). Lastly, the slant columns are divided by an air mass factor (AMF) to produce geophys-

20   ical HCHO vertical columns (independent of the satellite viewing geometry), which are then re-normalised using the HCHO background field from a chemical transport model. Reported final errors on gridded monthly mean vertical columns are approximately 20–60 % (De Smedt et al., 2008, 2012; Barkley et al., 2013), depending on the instrument and averaging method.

25   Over the oceans and regions with low HCHO, the vertical column error is mainly influenced by the slant column fitting error, whereas over continental enhancements, the errors associated with the AMF become more relevant. Given the primary use of HCHO columns is to constrain surface VOC emissions, it is therefore important to fully characterise the AMF and its error for each individual instrument and retrieval

Title Page

Abstract   Introduction

Conclusions   References

Tables   Figures

◄   ►

◄   ►

Back   Close

Full Screen / Esc

Printer-friendly Version

Interactive Discussion

(Barkley et al., 2012). The AMF represents observational sensitivity along the light path, relative to the vertical, accounting for the atmospheric and measurement state (Palmer et al., 2001). It is generally computed by a multiple-scattering radiative transfer model, using a priori information on aerosols, clouds, the HCHO vertical profile, and the surface reflectance, with the uncertainty of each influencing the final AMF error. Past studies, which have examined the HCHO AMF sensitivity to these parameters show the approximate errors associated with aerosols are 20–50 %, clouds 20–30 %, and surface reflectance 20 % (see, e.g., Palmer et al., 2006; Fu et al., 2007; De Smedt et al., 2008; Barkley et al., 2012). AMF errors arising from the HCHO profile vary depending on its relative vertical distribution to aerosols and clouds, but are of order 20–40 % (De Smedt et al., 2008; Barkley et al., 2012). The HCHO profile is also subject to chemistry transport model (CTM) errors, such as choice of BVOC emission inventory or chemical reaction scheme, which affect its accuracy (Barkley et al., 2012).

There is, therefore, a pressing need to improve AMF calculations and reduce uncertainties wherever possible. Accordingly, this paper details a new algorithm, which attempts to improve the accuracy of HCHO AMFs by performing scene-specific full-radiative transfer calculations and through more advanced treatment of the input a priori information. Furthermore, the algorithm includes a full radiative transfer error calculation for each observation, to help quantify AMF uncertainties and their corresponding spatial and temporal variation. The new AMF algorithm is applied to retrieved GOME-2 HCHO slant columns, to determine its subsequent impact on the tropospheric HCHO vertical columns.

The paper is structured as follows. Sections 2 and 3 provide an overview and a brief review of contemporary UV-Vis AMF calculations, respectively. Section 4 describes the default University of Leicester (UoL) GOME-2 AMF scheme, which establishes a reference to assess subsequent AMF updates. Section 5 outlines the major updates to the UoL AMF algorithm and assess their subsequent impact. An assessment of AMF errors is presented in Sect. 6. The paper concludes with a short summary.

2 Calculation of UV-Vis AMFs

The air mass factor for a given observation is defined as the ratio of the trace gas slant column density to its vertical column density. In a non-scattering atmosphere, the satellite viewing geometry dictates the light-path and hence a geometrical airmass factor (AMF_G) can be calculated by:

$$AMF_G = \frac{1}{\cos\theta_{SZA}} + \frac{1}{\cos\theta_{VZA}} \tag{1}$$

where θ_{SZA} and θ_{VZA} are the solar zenith and viewing-zenith angles, respectively. In the real atmosphere, Rayleigh scattering, and scattering from aerosols and clouds, strongly influence the photon path-length. To account for these effects, current UV-Vis trace gas retrievals typically calculate AMFs using the approach of Palmer et al. (2001), which decouples atmospheric scattering from the trace gas vertical profile, via:

$$AMF = AMF_G \int_0^\infty w(z)S(z)\,dz \tag{2}$$

where $w(z)$ are scattering weights that represent the sensitivity of the backscattered radiance to the absorber abundance at each altitude, and $S(z)$ is a normalised shape factor that describes the trace gas vertical distribution. The scattering weights are computed using a radiative transfer model (RTM), and are function of wavelength (λ), surface pressure (P_s), surface albedo (A) and the solar/viewing geometry; the shape factor is usually provided by an offline CTM. To account for partially cloudy scenes the approach of Martin et al. (2002) is commonly adopted, which assumes the total AMF is the reflectivity-weighted average of the air mass factors for the clear (AMF_{clr}) and cloudy (AMF_{cld}) pixel sub-scenes. Calculation of accurate AMFs therefore require each retrieval to select the best available a priori information, and the most suitable RTM and CTM. In the next section different approaches for calculating the AMFs are discussed.

3   Current AMF algorithms

While the basic method of calculation mostly remains the same for all AMFs (i.e. that of Palmer et al., 2001), AMF algorithms differ widely in the temporal and spatial resolution of a priori databases, choice of RTM, and their treatment of aerosols. Brief summaries of state-of-the-art HCHO and analogous tropospheric nitrogen dioxide (NO_2) AMF algorithms are presented in Tables 1 and 2, respectively.

The importance of using an accurate and spatially resolved surface reflectance product in AMF calculations has been cited as one of the most significant factors in reducing AMF error (Boersma et al., 2004; Zhou et al., 2010). Highly reflecting surfaces increase measurement sensitivity to boundary layer trace gases, whereas the converse is true for dull surfaces. Thus, an ideal albedo dataset must resolve fine-scale features, otherwise calculated AMFs will be erroneous. For example, a MODIS $0.05° × 0.05°$ 16 day mean albedo product is utilised in the OMI NO_2 retrieval by Russell et al. (2011), since it removes artificial NO_2 features evident when a coarser GOME $1° × 1°$ albedo climatology is used. Albedo data sets currently available include: Herman and Celarier (1997), Koelemeijer et al. (2003), or a combination of the two, e.g., Boersma et al. (2004). More recent HCHO retrievals (e.g., De Smedt et al., 2012; González Abad et al., 2014), use the Kleipool et al. (2008) monthly albedo climatology derived from OMI. Unfortunately, no GOME-2 specific albedo data sets are currently available; surface reflectances applied for HCHO AMF calculations are derived from satellite instruments with observation times different from that of GOME-2. Popp et al. (2011) suggest application of the $0.25° × 0.25°$ MEdium Resolution Imaging Spectrometer (MERIS) black sky albedo product at 416 nm to UV-vis NO_2 vertical column retrievals, offering potential for an extrapolation of the dataset, whose local overpass time of 10:30 better matches that of GOME-2 at 09:30 than other available products, to lower HCHO relevant wavelengths using techniques demonstrated for the (Kleipool et al., 2008) albedo product. Similar albedo products which may be of use for downscaling in wavelength to the HCHO fitting range include MODIS black sky as used in the Russell et al. (2011) study, and

MISR albedomap products, although flying as part of the NASA A-train implies a local overpass of 13:30, imparts problems of temporal applicability already noted for the OMI Kleipool et al. (2008) dataset.

Trace gas a priori profiles are usually taken from a CTM, or alternatively a climatology. Retrieval groups differ in their CTM choice, whose complexity often varies, using spatial resolutions ranging from a few km^2 (Heckel et al., 2011; Russell et al., 2011) in regional studies to 4° × 5° for global use (De Smedt et al., 2008; Hewson et al., 2013). Monthly mean or daily profiles can be used, although the latter is expected to provide a more detailed evolution of tropospheric chemistry. For example, Valks et al. (2011) found NO_2 AMF uncertainties of about 10 % due to monthly CTM fields by comparing against daily values calculated over the same time period. Most advanced AMF schemes also adjust the trace gas profile according to the mean elevation over the satellite footprint to remove biases arising from inaccurate terrain pressure, using the surface pressure correction devised by Zhou et al. (2009). Studies have shown that for NO_2 this correction can cause differences of about ±20 % in the tropospheric column (Schaub et al., 2007; Zhou et al., 2009; Boersma et al., 2011a; Russell et al., 2011).

Aerosol scattering and absorption can have significant impacts on HCHO observations (Fu et al., 2007; Gonzi et al., 2011; Barkley et al., 2012). In particular, biomass burning aerosols distributed high above the boundary layer can artificially enhance tropospheric vertical columns by up to 50 % (Barkley et al., 2012). Current algorithms either explicitly correct for aerosol effects using modelled aerosol optical depth (AOD) profiles and properties (e.g., Barkley et al., 2012, 2013), or alternatively, implicitly rely on corresponding cloud algorithms to correct for their presence (e.g., De Smedt et al., 2008, 2012; Boersma et al., 2011a). Nevertheless, further detailed investigation is required to fully understand aerosol effects on current tropospheric UV-Vis retrievals.

Finally, retrievals either derive AMFs from pre-calculated look up tables (LUT), or calculate an individual AMF for each observation. Scene-specific AMFs are expected to be more accurate since they tend to incorporate more representative a priori information and do not suffer from potential LUT interpolation errors, however, their calculation

often requires considerable computational expense. Additionally, AMF errors are either estimated from error LUTs (e.g., De Smedt et al., 2008), sensitivity studies (e.g., Valks et al., 2011), or in the worst case simply quoted from relevant past studies, rather than being explicitly calculated by the RTM for each observation over the region of interest.

4 The UoL GOME-2 HCHO retrieval

4.1 Slant column retrieval

GOME-2 HCHO slant columns used in this work come from Hewson et al. (2013). In brief, slant columns are calculated with the DOAS method (Platt and Stutz, 2008), using the QDOAS analysis package (Fayt et al., 2011). The cross-sections of HCHO and interfering absorbers (BrO, O_3 and NO_2), as well as Ring and undersampling contributions, are fitted to GOME-2 measured line of sight radiances after removal of broadband absorption terms with a 5th order polynomial. Biases in the slant columns are removed using a reference sector method, by fitting a daily latitudinal polynomial to measured HCHO columns over the Pacific Ocean, between 170–140° W. This latitudinal area corresponds to a region where the only background levels of HCHO occur due to methane oxidation. The polynomial is subtracted from all global measurements, and then AMFs calculated and applied to obtain vertical columns, which are then renormalised through addition of corresponding model HCHO columns from the same Pacific region. In the UoL retrieval, the model fields are provided by the GEOS-Chem CTM, as described in Hewson et al. (2013). Details of the GEOS-Chem simulation and the baseline University of Leicester (UoL) AMF algorithm, which explicitly calculates an AMF for each observation, are discussed in the next sections.

4.2 GEOS-Chem chemical transport model

The GEOS-Chem chemical transport model (version 08-03-01) is used to simulate tropospheric chemistry at global and regional scales, and to provide daily a priori tropo-

Title Page

Abstract | Introduction

Conclusions | References

Tables | Figures

◀ | ▶

◀ | ▶

Back | Close

Full Screen / Esc

Printer-friendly Version

Interactive Discussion

spheric HCHO and AOD profiles, appropriate to GOME-2's local overpass time (09:00–10:00). The model is driven by meteorological fields provided by NASA's Goddard Earth Observing System version 5 (GEOS-5) assimilation system (Rienecker et al., 2008), which are available at a native spatial resolution of 0.5° latitude × 0.67° longitude, and with 72 vertical pressure levels from the surface to 0.01 hPa. However, the resolution of the GEOS-5 data is degraded accordingly to 2° × 2.5° and 4° × 5°, to run GEOS-Chem globally at medium and coarse spatial scales. Additionally, over tropical South America where isoprene emissions are large and HCHO columns high, GEOS-Chem is also employed in a one-way nested grid mode, utilising GEOS-5 default resolution to better resolve features in this key region (see Barkley et al., 2011). To ensure consistency, boundary conditions for nested South America simulation are provided by the 4° × 5° model run. In each model configuration the vertical dimensions are also degraded to 47 pressure levels, with the lowermost layers of the model (surface ≤ 2 km) approximated by 14 layers.

GEOS-Chem simulates tropospheric photochemistry taking into account major chemical species (O_3, NO_x and VOCs) and aerosol interactions, with a reaction scheme which consists of about 400 reactions and 80 species based on the work of Paulot et al. (2009a, b) and Mao et al. (2013). Relevant input emission inventories include the MEGAN biogenic VOC database (Guenther et al., 2006), EDGAR anthropogenic emissions (Olivier et al., 2001), and the Global Fire Emissions Database v2 (van der Werf et al., 2006). Anthropogenic emissions are overwritten with more detailed regional inventories where possible, as described in van Donkelaar et al. (2008). A detailed account of the tropical South America simulation, including updates to the chemical and dry deposition schemes which are applied in all simulations, can be found in Barkley et al. (2011).

4.3 Baseline AMF calculation

The baseline UoL AMF calculation uses daily data from the global GEOS-Chem 4° × 5° simulation, with model quantities sampled at the same time and location of each ob-

servation. In this study the scattering weights and sub-scene reflectivities are generated for each observation with the LIDORT v2.3 radiative transfer model (Spurr, 2002), following Palmer et al. (2001) and Martin et al. (2002). In addition to HCHO, other atmospheric profiles used within LIDORT include GEOS-Chem AOD profiles (for mineral dust, tropospheric sulphate, black carbon, organic carbon and sea salt), and also US standard atmosphere O_3 and NO_2 profiles. AMFs are computed at a wavelength of 340 nm, representative of the DOAS HCHO slant column fitting region (328.5–346 nm) (Barkley et al., 2012; Hewson et al., 2013), and consistent with the Herman and Celarier (1997) Lambert equivalent reflectivity database used at 360 nm, and CTM AODs at 340 nm calculated with physical aerosol optical properties based on the study of Martin et al. (2003). Cloud fraction and cloud top pressure are taken from the most recent version of the GOME-2 FRESCO+ cloud product (Wang et al., 2008), using the Popp et al. (2011) MERIS albedo climatology for surface reflectivity values in the O_2 A-band retrieval. FRESCO+ does not calculate cloud optical thickness (COT) values, thus clouds are treated as Lambertian reflectors with an albedo of 0.8, a method consistent with other studies (e.g., De Smedt et al., 2012; Barkley et al., 2013; González Abad et al., 2014). Monthly climatological maps of the ~ 360 nm surface albedo, taken from the TOMS Lambert equivalent reflectivity (LER) database (November 1978–May 1993) generated by Herman and Celarier (1997), are re-gridded to match the GEOS-Chem grid and used in clear-sky conditions.

Following Martin et al. (2003), we account for aerosols in the AMF calculation by representing within the LIDORT model their vertically resolved optical properties from the GEOS-Chem simulation described in Sect. 4.2. In practice height resolved AODs are used for the aerosol extinction (i.e. per km); for aerosol scattering the AODs are weighted by the appropriate single scattering albedo (SSA) of that aerosol type. Aerosol optical properties (black and organic carbon aerosols, mineral dust, sulphate, sea salt and water vapour) are based on the GADS (Global Aerosol Data Set) data (Köpke et al., 1997). Tabulated values are calculated offline and implemented into GEOS-Chem, as described in Martin et al. (2003). Values consistent with GEOS-Chem

are also used directly in the AMF computation. In the AMF calculation itself, a humidity of 70 % is assumed and we use values specific to 340 nm, of the extinction efficiency, effective radius, SSA and the first eight terms in the Legendre expansion of the phase function (π). At 340 nm, the SSAs of the aerosols types are 0.2342, 0.9861, 0.8394, 1.0, 1.0 and 1.0 respectively.

Using these default settings, scene-specific GOME-2 AMFs are calculated for March and August 2007, months chosen to both reflect the range of expected tropospheric HCHO concentrations, and provide a reference for subsequent comparisons. Figure 1 shows gridded monthly mean AMFs and HCHO vertical columns calculated from the reference sector corrected slant columns derived for the two selected months. Calculated AMFs are 0.55–3.68 over the ocean, and 0.61–3.68 over land. Observed HCHO columns in March are generally low, whilst in August seasonal enhancements are evident over the southeast US and the Amazon rainforest, features consistent with other GOME-2 retrievals (De Smedt et al., 2012).

5   UoL AMF algorithm updates

5.1   Overview

To improve the UoL AMF algorithm six main updates have been applied and evaluated. These are: (1) assessment of different GEOS-Chem grid resolutions; (2) area-weighting of a priori inputs to match the satellite footprint; (3) an upgrade of the surface albedo database; (4) application of the Zhou et al. (2009) terrain correction, (5) the HCHO and ozone absorption cross sections within LIDORT have been changed to match those used in the slant column retrieval, and are adjusted to account for change of GOME-2's slit function over time and also for temperature effects, and finally (6) the US Standard O_3 vertical mixing ratios are replaced with climatology based values and scaled with coincident GOME-2 total column O_3 observations. The results of these improvements are as follows.

5.2   Impact of GEOS-Chem grid resolution

Low resolution input databases can lead to inaccurate AMF calculations due to mis-representation of small scale surface features, especially over rapidly changing terrain such as land-sea boundaries and mountainous regions (Boersma et al., 2007, 2011a; Heckel et al., 2011; Russell et al., 2011; Lin et al., 2014). A nominal GOME-2 pixel covers $80\,km \times 40\,km$ footprint on the Earth's surface, considerably smaller than the default GEOS-Chem $4° \times 5°$ simulation, as shown in Fig. 2. Reducing potential errors from this mis-match in spatial scale requires the use of a priori information at spatial resolutions equivalent to, or higher, than the satellite footprint. Hence in addition to the coarse $4° \times 5°$ simulation, GEOS-Chem is used to generate HCHO and AOD pro-files globally at $2° \times 2.5°$ and for tropical South America at $0.5° \times 0.667°$ to assess their subsequent impact on corresponding HCHO AMFs.

Figure 3 shows the spatial maps and histograms of the AMF percentage difference (relative to the default case) resulting from use of HCHO and AOD profiles from the high resolution GEOS-Chem Amazon nested grid. AMFs can vary from $\pm 20\,\%$, with the largest changes typically found at the edges of coarse grid cells, along coastlines, and over mountainous regions, reflecting the ability of the nested-model to better cap-ture HCHO spatial variations over changing terrain. Similarly, AMF differences arising from use of global $2° \times 2.5°$ profile data are slightly smaller, typically $\pm 10\,\%$, with the biggest differences again over grid cell boundaries, coastlines, and mountain regions. The magnitude of the AMF differences therefore increases with higher spatial model resolution. Hence to reduce unnecessary errors, data users focussing on regional stud-ies should aim to recalculate AMFs using profile information which can resolve the spatial characteristics of their target domain.

5.3   Impact of footprint area weighting

A pure grid cell selection algorithm (hereafter referred to as "IJ"), which uses the ob-servation centre coordinates to select the most appropriate a priori data, can lead to

Title Page

Abstract | Introduction

Conclusions | References

Tables | Figures

|◄ | ►|

◄ | ►

Back | Close

Full Screen / Esc

Printer-friendly Version

Interactive Discussion

representation errors by not accounting for satellite pixels that overlap multiple model grid-cells. To overcome this issue an area-weighted mean value (AWM) for each scan is calculated based on the areal proportions of GEOS-Chem grid cells underlying the satellite footprint. The area-weighted values of all gridded AMF inputs (surface pressure and model profiles) are computed using a tessellation algorithm originally developed by Spurr (2003) for GOME and SCIAMACHY operational processing. Before calculation of average area-weighted profile quantities, all model profiles within the satellite footprint are first interpolated onto a common vertical pressure grid, based on the area-weighted surface pressure, to account for pressure level differences between neighbouring GEOS-Chem grid cells. The total AOD is persevered by scaling the final profile accordingly.

To evaluate this method the area-weighting technique was first applied to all three GEOS-Chem model simulations independently, and compared to the corresponding results when the IJ method is applied to the same model grid resolution. In all three cases, use of AWM model profiles changes the AMFs by about ±2.5 % for about 85–95 % of locations, i.e. only a small difference overall. If AMFs, calculated using AWM model profiles from GEOS-Chem's nested-grid $0.5° \times 0.667°$ simulation, are then compared to AMFs from the default UoL algorithm, the effect of the AWM is also small and less than the effect of using the nested grid profiles alone, as shown by the green and blue lines, respectively, in the histograms of Fig. 3. Hence for GOME-2, the effect on the AMFs from using higher resolution model data is greater than effects from area-weighting model quantities. This is also true globally when both IJ and AWM model profiles from GEOS-Chem's $2° \times 2.5°$ profile are compared to the default UoL algorithm (not shown). Nevertheless, the area-weighting of model profiles still represents a small but important correction for those observations straddling multiple model grid-cells.

5.4 Impact of surface pressure correction

Accurate surface pressure values are a critical component in defining the trace gas vertical distribution. Zhou et al. (2009) presented a modification to regional NO_2 AMF

calculations, to mitigate for terrain bias in mountainous regions due to inadequate topography representation. Accordingly, this terrain pressure correction is also applied here for HCHO. Following the terminology of Zhou et al. (2009), the 0.0083° × 0.0083° GMTED2010 Digital Elevation Model (DEM) (Danielson and Gesch, 2011), is used to calculate h_{eff}, an area-weighted effective terrain height for each GOME-2 observation. Similarly, corresponding area-weighted model values of surface temperature (T_{surf}), original surface pressure (p_{CTM}) and CTM terrain height (h_{CTM}) are also computed for each scan. To perform the correction, an effective surface pressure p_{eff} is first derived:

$$p_{eff} = p_{CTM} \times \left(\frac{T_{surf}}{T_{surf} + \Gamma \times (h_{CTM} - h_{eff})} \right)^{-g/r\Gamma}, \tag{3}$$

with Γ the adiabatic lapse rate of $6.5\,\mathrm{K\,km^{-1}}$, g as gravitational acceleration at $9.8\,\mathrm{m\,s^{-2}}$, and r dry air gas constant of $287\,\mathrm{J\,kg^{-1}\,K^{-1}}$. From this, the tops and bottoms of the model pressure layers l are defined for p_{eff} and p_{CTM}, using GEOS-5's eta (η) vertical coordinate:

$$\begin{aligned} p_{CTM_b}(l) &= \eta_A(l) + p_{CTM} \times \eta_B(l) \\ p_{CTM_t}(l) &= \eta_A(l+1) + p_{CTM} \times \eta_B(l+1) \\ p_{eff_b}(l) &= \eta_A(l) + p_{eff} \times \eta_B(l) \\ p_{eff_t}(l) &= \eta_A(l+1) + p_{eff} \times \eta_B(l+1) \end{aligned} \tag{4}$$

where the η_A and η_B are the GEOS-5 coefficients that define the pressure levels. A scaling factor, to conserve mixing ratios when interpolating to the new pressure grid, is calculated from:

$$p_{eff_{scl}}(l) = \frac{p_{eff_b}(l) - p_{eff_t}(l)}{p_{CTM_b}(l) - p_{CTM_t}(l)}. \tag{5}$$

Model HCHO profiles are then transferred to the new p_{eff} grid, and scaled with $p_{eff_{scl}}$; AOD profiles are also interpolated to the new grid and the total column AODs preserved. Figure 4 details an example HCHO profile before, and after, the application of the pressure correction, with the shape and amount of the vertical profile changing as a function of the scaling value derived for the new pressure grid; in this instance the AMF decreases by about 4 %. To illustrate the effect of the pressure correction on a scan by scan basis, individual GOME-2 orbits over the Amazon are presented in Fig. 5. To isolate the effect of the pressure correction, AMFs calculated with area weighted GEOS-Chem inputs from the default algorithm are shown in the top left plot. For these orbits, adjusting the coarse resolution $4° \times 5°$ surface pressure grids with the high resolution GMTED surface elevation data produces AMF differences of up to ±5 %, mostly over areas of rapidly changing terrain (e.g., over the Andes mountains). However, when surface pressure correction is applied to the GEOS-Chem $0.5° \times 0.667°$ nested grid profiles, the effect is smaller as the GEOS-5 surface pressures more accurately represent the surface topography. This is confirmed by the histograms shown in Fig. 3, which reveals the impact area-weighting (green line) and the subsequent pressure correction (aqua line) are small, in comparison to the effect of using the $0.5° \times 0.667°$ nested grid profiles alone (blue line).

5.5 Impact of new OMI surface albedo product

The baseline UoL AMF algorithm uses the surface albedo maps from the Herman and Celarier (1997) database. Choice of surface albedo data is critical since it can cause 20 % changes in retrieved tropospheric HCHO and NO_2 columns (Zhou et al., 2010; Barkley et al., 2012). Bi-directional distribution function (BRDF) effects associated with the surface reflectance are less than < 5 % for NO_2 (Zhou et al., 2010), but unfortunately for HCHO cannot be assessed owing to the lack of a BDRF product at relevant wavelengths.

To improve the UoL AMF algorithm the surface albedo is upgraded to the OMI $0.5° \times 0.5°$ database generated by Kleipool et al. (2008), using surface reflectance data

at 342 nm. Furthermore, daily changes in surface albedo are accounted for using linear interpolation between months, following the approach of Boersma et al. (2011b), and with the area-weighting procedure described in Sect. 5.3 also applied.

Compared with the TOMS data, ocean albedos are generally higher with the OMI product, whilst over land, albedos are also generally higher, with the exceptions of the Sahara, high northern latitudes, and much of the boreal landmass in March (not shown). Consequently, AMF differences reflect these albedo changes, as shown in Figure S3. Relative to the default UoL AMF algorithm, about 70 % of locations show an AMF increase of up to 5 %, and about 25 % of locations show a decreases of up to 5 %.

5.6 Impact of GOME-2 cross-sections

The baseline AMF implementation generates scattering weights with HCHO using absorption spectra based on Cantrell et al. (1990). This is improved on by passing the HCHO (Meller and Moortgat, 2000), and ozone (Malicet et al., 1995), cross-sections from the slant column fitting of the GOME-2 retrieval, convolved to the current orbit's asymmetric slit function, additionally allowing for the time-dependent slit function degradation throughout the instrument's lifetime (e.g., Cai et al., 2012; Dikty and Richter, 2012). Furthermore, the HCHO and ozone cross-sections are adjusted to the local temperature profile, via cited temperature coefficients. However, the result of this algorithm update is minor, causing a fairly uniform global decrease in AMFs of between 0–2 %.

5.7 Impact of TOMS ozone climatology

In the baseline UoL AMF algorithm, O_3 vertical mixing ratios are fixed to a single profile representing the US standard summertime atmosphere, thus any major O_3 spatial and temporal variations are ignored in the AMF computation. Using a fixed O_3 profile is therefore likely to introduce errors through incorrect scattering weight values, particu-

Title Page

Abstract | Introduction

Conclusions | References

Tables | Figures

Back | Close

Full Screen / Esc

Printer-friendly Version

Interactive Discussion

larly significant for weak absorbers such as HCHO. To overcome this issue, the fixed US O_3 profile is replaced by a climatology derived from TOMS version 8 O_3 (Bhartia, 2002) data, as applied in the SCIATRAN v2.2 radiative transfer model (Rozanov et al., 2005). The TOMS v8 climatology provides monthly O_3 VMRs in eighteen 10° latitude bands for 61 atmospheric levels. To account for concurrent O_3 variability, each selected TOMS v8 profile is interpolated onto the pressure grid based on the AWM surface pressure, and then scaled to coincident GOME-2 O_3 total column measurements, provided by the operational DLR retrieval (Loyola et al., 2011). Note a similar scaling of the US ozone profile was also performed by Lee et al. (2009) in the computation of OMI SO_2 AMFs.

Results of the ozone profile substitutions are presented in Figure S4, which shows that whilst the magnitude of the AMF differences are small, mostly within ±2 %, the variation is geographically widespread. The most notable changes occur over regions of high surface elevation (>1500 m) where divergence between the US standard atmosphere and TOMS v8 ozone profiles, relative to the HCHO profile peak are most pronounced.

5.8 Combined effect of all AMF updates

To produce an improved airmass factor calculation the updates presented are combined in a new UoL AMF algorithm, as summarised in Table 3. In future, global processing of the GOME-2 HCHO columns (as here), will rely on using GEOS-Chem model data at 2° × 2.5° resolution, whereas studies focussing on tropical South America will utilise output from the Amazon nested-grid simulation. Figure 6 shows the differences of the new AMF algorithm against the initial baseline implementation. On a single Intel Xeon X5550 running at 2.67 GHz, per-orbit processing time for the AMF calculations including all algorithm modifications is between 15–20 min (increased on 7–8 min per orbit for the baseline method), reflecting extra time spent applying pixel tessellation routines to input grids. Typically differences between the original IJ algorithm and the updated AMF calculations are of order ±10 % with the biggest changes occur-

ring over mountain regions, coastlines and the grid-cell outlines of the GEOS-Chem $2° \times 2.5°$ and $4° \times 5°$ horizontal grids. Cancellation of opposing effects from individual algorithm changes mitigates the magnitude of the overall difference. The overall impact of the AMF updates is therefore to mainly improve the tropospheric vertical column retrievals over regions with rapidly changing surface elevation and terrain properties. AMFs from the updated UoL algorithm are now 0.52–2.89 over land and 0.62–3.93 over the oceans. Interestingly, in August 2007 there is a significant reduction in the AMFs over the mid-Atlantic, and over the Arabian sea, just south of the Yemen and Oman coastlines. These features are spatially coincident with elevated dust AODs from GEOS-Chem, reflecting the simulated aerosol field sensitivity to the model's spatial resolution, and its subsequent effect on the AMF. These findings correlate with the implicit AMF aerosol correction sensitivity tests in Barkley et al. (2012), where aerosol corrections were shown to impart only minor effects on HCHO vertical columns over photochemically active regions ($< 15\%$), with larger effects noted for regions containing significant quantities of desert dust, and biomass burning regions.

6 AMF error assessment

Any AMF algorithm should properly characterise its error. Following Boersma et al. (2004) and De Smedt et al. (2008), the AMF total error (σ_{AMF}) may be expressed as:

$$\sigma_{\text{AMF}}^2 = \left(\frac{\partial \text{AMF}}{\partial A_s}\sigma_{A_s}\right)^2 + \left(\frac{\partial \text{AMF}}{\partial \text{CF}}\sigma_{\text{CF}}\right)^2 + \left(\frac{\partial \text{AMF}}{\partial \text{CTP}}\sigma_{\text{CTP}}\right)^2 + \left(\frac{\partial \text{AMF}}{\partial S}\sigma_{\text{S}}\right)^2. \tag{6}$$

where σ_{A_s}, σ_{CF}, σ_{CTP}, and σ_{S} are the uncertainties associated with the surface albedo, cloud fraction, cloud-top pressure, and the HCHO shape profile, and the partial derivatives indicate the local AMF sensitivity with respect to each parameter. For the en-

tire GOME-2 record (2007–2012) the AMF errors are explicitly calculated for each observation (using the updated algorithm) through assigning the following uncertainties: $\sigma_{A_s} = 0.05$, $\sigma_{CF} = 0.05$, and $\sigma_{CTP} = 60$ hPa, based on relevant studies (see e.g., Kleipool et al., 2008; Wang et al., 2008), and then by applying these uncertainties to

5 determine the local AMF sensitivity, i.e. by generating partial derivatives of the radiance fields with respect to these sources of model error using LIDORT. Quantification of the profile uncertainty σ_S, is difficult to assess, since the HCHO vertical distribution is influenced by many complex processes (e.g., transport, chemistry, and boundary layer height). Hence in the case of the HCHO profile shape, the error and local sensitivity

10 are estimated by perturbing the HCHO profiles below and two model layers above the simulated HCHO peak by +25 %, whilst layers above these are decreased by −25 %. Modifying the HCHO profile in this way also provides a partial assessment of AMF uncertainties due to the presence of aerosols, since their relative vertical distribution has changed. However, without precise information on the aerosol distribution and optical

15 properties it is extremely difficult to accurately quantify aerosol induced errors; simply adjusting the GEOS-Chem aerosol profiles only provides a limited insight into this error source (e.g., Barkley et al., 2012).

    Figures 7 and 8 show total and individual component errors respectively, revealing AMF uncertainty varies considerably both in magnitude and distribution. The greatest

20 source of AMF uncertainty by far, is associated with the HCHO profile shape, with median errors of order 50 %. HCHO profiles are particularly large where low-lying cloud occurs, e.g., off the west coast of South America in August, owing to cloud albedo and shielding effects. A further AMF calculation, in which the reverse scaling to the a priori HCHO profile was also performed, resulted in similar but more widespread errors. In

25 comparison, average uncertainties due to cloud top pressure and cloud fraction are both about 10 %, whilst those associated the surface albedo are about 5 %. Median AMF total errors are therefore approximately 50–60 %, consistent with those found previously for the SCIAMACHY and OMI instruments by Barkley et al. (2012). However,

for individual observations GOME-2 AMF errors can range from 5–600 % depending on the immediate local conditions.

Figure 9 shows the seasonal variability of the AMF and its error over two key regions: the southeast USA and tropical South America. In general, the mean and minimum AMFs show little variation over the five year period for either region, whereas the maximum AMFs show some seasonal deviations. For both regions, the total AMF error is dominated by the uncertainty associated with the a priori HCHO profiles. AMF errors over tropical South America also do not vary significantly, owing to copious biogenic emissions from the rainforest sustaining high levels of HCHO all year round. In contrast, the AMF errors over the southeast USA, however, have a distinct seasonal pattern with low AMF errors in winter when biogenic emissions and HCHO levels are a minimum, and high AMF errors in summer, when HCHO concentrations peak due to significant isoprene emissions (Palmer et al., 2006). Thus, any top-down estimates of isoprene emissions over North America are likely to be compromised by large AMF errors in the months of highest emissions. Examination of other regions (not shown), also confirms that any variance in the AMF errors is predominantly driven by biogenic emission seasonality influencing the HCHO profile shape.

6.1 Aerosol effect on AMF errors

In their assessment of HCHO AMF uncertainty, Barkley et al. (2012) conducted an extensive investigation into AMF sensitivity to AOD over the Amazon region for both SCIAMACHY AND OMI HCHO AMFs. Their series of tests included calculating AMFs with no aerosol correction, arbitrary AOD scaling, and redistribution of black carbon (BC) and OC to various heights above the boundary layer dependent on AMF peak layer AOD residing in the boundary layer. Results from this work showed HCHO AMFs were only significantly affected (in a range of 10–50 %) when BC and organic carbon were distrbuted high above the boundary layer to approximately 5 km. For a basic indication of aerosol errors in this work we therefore include a brief investigation on the effect of aerosol on our GOME-2 specific AMFs. Testing of aerosol effects are limited

to BC, given the sensitivity of HCHO AMFs to the species shown in Fu et al. (2007) and Barkley et al. (2012).

To this end, we identified scans whose a-priori GEOS-Chem BC AOD profile peaks within 2 km of Earth's surface, and increased their AOD values between the surface and 5 km to the maximum BC AOD for that scan. Smearing the AOD profile to heights well above the planetary boundary layer where the bulk of HCHO resides, generates an artifical BC interference in the AMF calculation with AOD values in keeping with those expected for the scene, but significantly perturbed to provide a gauge on AMF error due to BC AOD profile. Scans with a-priori BC profile peaks above this height criteria are assigned a default error of 20 %, in keeping with the default HCHO VMR error (also provided by GEOS-Chem, with expected similar transport errors between the two species).

Estimated mean AMF error due to BC for the two tested months are plotted in Figure S3, displaying minimum errors around 15–20 %, and median maximums in the range of 50–75 %, showing consistency with values reported in Barkley et al. (2012). Increased BC AMF error values exhibit a very similar spatial pattern to HCHO profile errors in Fig. 8, suggesting the relative distribution of the two components is key for understanding the aerosol AMF error source.

7 Summary

This work has presented and evaluated a new University of Leicester algorithm to compute HCHO AMFs for the GOME-2 instrument. The most novel aspects of the new algorithm are the area-weighting of improved a priori information over the satellite footprint, to more accurately represent the local surface conditions and atmospheric state, and the full radiative transfer calculation of the AMF and its error for each GOME-2 observation. Compared to an earlier UoL AMF code, the new algorithm typically changes calculated AMFs by up to ±10 %, with the largest changes over coastal and mountain regions, and the model cell boundaries of the GEOS-Chem horizontal grids. The

Title Page

Abstract | Introduction

Conclusions | References

Tables | Figures

◄ | ►

◄ | ►

Back | Close

Full Screen / Esc

Printer-friendly Version

Interactive Discussion

greatest impact on the AMFs arises from using HCHO profiles from a high resolution GEOS-Chem 0.5° × 0.667° nested grid simulation in preference to those from coarser global simulations. Furthermore, it is found that (a) the largest AMF error component is also associated with the HCHO profile shape, and (b) seasonal variations in the total AMF error are driven by seasonal changes in the HCHO profile distribution. These results therefore highlight the critical importance of accurate and high-resolution profiles within the GOME-2 AMF calculation, or for that matter, any other HCHO retrieval. In addition, users of HCHO data products should be fully aware of seasonal shifts in the AMF error, and the likely impact on any inferred top-down emission estimates.

Ongoing efforts are being conducted to validate and develop a full-error analysis of the UoL GOME-2 HCHO tropospheric column product, to provide confidence in its use for inversion studies of surface VOC emissions. Further algorithm refinement to potentially improve retrievals in the presence of aerosols and over snow covered surfaces are also being investigated.

The Supplement related to this article is available online at doi:10.5194/amtd-8-1109-2015-supplement.

References

Barkley, M. P., Palmer, P. I., Kuhn, U., Kesselmeier, J., Chance, K., Kurosu, T. P., Martin, R. V., Helmig, D., and Guenther, A.: Net ecosystem fluxes of isoprene over tropical South America inferred from GOME observations of HCHO columns, J. Geophys. Res., 113, D20304, doi:10.1029/2008JD009863, 2008. 1111

GOME-2 airmass factors

W. Hewson et al.

Title Page

Abstract	Introduction
Conclusions	References
Tables	Figures

|◄ | ►|

◄ | ►

| Back | Close |

Full Screen / Esc

Printer-friendly Version

Interactive Discussion

Barkley, M. P., Palmer, P. I., Ganzeveld, L., Arneth, A., Hagberg, D., Karl, T., Guenther, A., Paulot, F., Wennberg, P. O., Mao, J., Kurosu, T. P., Chance, K., Müller, J.-F., Smedt, I. D., Roozendael, M. V., Chen, D., Wang, Y., and Yantosca, R. M.: Can a "state of the art" chemistry transport model simulate Amazonian tropospheric chemistry?, J. Geophys. Res., 116, D16302, doi:10.1029/2011JD015893, 2011. 1117

Barkley, M. P., Kurosu, T. P., Chance, K., Smedt, I. D., Roozendael, M. V., Arneth, A., Hagberg, D., and Guenther, A.: Assessing sources of uncertainty in formaldehyde air-mass factors over tropical South America: implications for top-down isoprene emission estimates, J. Geophys. Res., 117, D13304, doi:10.1029/2011JD016827, 2012. 1112, 1115, 1118, 1123, 1126, 1127, 1128, 1129

Barkley, M. P., Smedt, I. D., Van-Roozendael, M., Kurosu, T. P., Chance, K., Arneth, A., Hagberg, D., Guenther, A., Paulot, F., Marais, E., and Mao, J.: Top-down isoprene emissions over tropical South America inferred from SCIAMACHY and OMI formaldehyde columns, J. Geophys. Res.-Atmos., 118, 6849–6868, doi:10.1002/jgrd.50552, 2013. 1111, 1115, 1118, 1139

Bhartia, P. K.: TOMS-V8 Total O_3 Algorithm Theoretical Basis Document, OMI Algorithm Theoretical Basis Document, NASA Goddard Space Flight Center, Greenbelt, Maryland, USA, 2002. 1125

Boersma, K. F., Eskes, H. J., and Brinksma, E. J.: Error analysis for tropospheric NO_2 retrieval from space, J. Geophys. Res., 109, D04311, doi:10.1029/2003JD003962, 2004. 1114, 1126, 1140

Boersma, K. F., Eskes, H. J., Veefkind, J. P., Brinksma, E. J., van der A, R. J., Sneep, M., van den Oord, G. H. J., Levelt, P. F., Stammes, P., Gleason, J. F., and Bucsela, E. J.: Near-real time retrieval of tropospheric NO_2 from OMI, Atmos. Chem. Phys., 7, 2103–2118, doi:10.5194/acp-7-2103-2007, 2007. 1120

Boersma, K. F., Eskes, H. J., Dirksen, R. J., van der A, R. J., Veefkind, J. P., Stammes, P., Huijnen, V., Kleipool, Q. L., Sneep, M., Claas, J., Leitão, J., Richter, A., Zhou, Y., and Brunner, D.: An improved tropospheric NO_2 column retrieval algorithm for the Ozone Monitoring Instrument, Atmos. Meas. Tech., 4, 1905–1928, doi:10.5194/amt-4-1905-2011, 2011a. 1115, 1120, 1140

Boersma, K. F., Braak, R., and van der A, R. J.: Dutch OMI NO_2 (DOMINO) data product v2.0, HE5 data file user manual, 2011b. 1124

Title Page

Abstract | Introduction

Conclusions | References

Tables | Figures

◀ | ▶

◀ | ▶

Back | Close

Full Screen / Esc

Printer-friendly Version

Interactive Discussion

Cai, Z., Liu, Y., Liu, X., Chance, K., Nowlan, C. R., Lang, R., Munro, R., and Suleiman, R.: Characterization and correction of Global Ozone Monitoring Experiment 2 ultraviolet measurements and application to ozone profile retrievals, J. Geophys. Res.-Atmos., 117, 2156–2202, doi:10.1029/2011JD017096, 2012. 1124

5 Cantrell, C. A., Davidson, J. A., McDaniel, A. H., Shetter, R. E., and Calvert, J. G.: Temperature-dependent formaldehyde cross sections in the near-ultraviolet spectral region, J. Phys. Chem., 94, 3902–3908, 1990. 1124

Chance, K.: OMI Algorithm Theoretical Basis Document, Volume IV, OMI Trace Gas Algorithms, OMI-ATBD-VOL4, ATBD-OMI-04, Version 2.0, 2002.

10 Chance, K., Palmer, P. I., Spurr, R. J. D., Martin, R. V., Kurosu, T. P., and Jacob, D. J.: Satellite observations of formaldehyde over North America from GOME, Geophys. Res. Lett., 27, 3461–3464, doi:10.1029/2000GL011857, 2000. 1111

Curci, G., Palmer, P. I., Kurosu, T. P., Chance, K., and Visconti, G.: Estimating European volatile organic compound emissions using satellite observations of formaldehyde from the Ozone
15 Monitoring Instrument, Atmos. Chem. Phys., 10, 11501–11517, doi:10.5194/acp-10-11501-2010, 2010. 1111

Danielson, J. and Gesch, D.: Global Multi-resolution Terrain Elevation Data 2010 (GMTED2010), Open-File Report 2011–1073, US Geological Survey, 2011. 1122

De Smedt, I., Müller, J.-F., Stavrakou, T., van der A, R., Eskes, H., and Van Roozendael, M.:
20 Twelve years of global observations of formaldehyde in the troposphere using GOME and SCIAMACHY sensors, Atmos. Chem. Phys., 8, 4947–4963, doi:10.5194/acp-8-4947-2008, 2008. 1111, 1112, 1115, 1116, 1126

De Smedt, I., Van Roozendael, M., Stavrakou, T., Müller, J.-F., Lerot, C., Theys, N., Valks, P., Hao, N., and van der A, R.: Improved retrieval of global tropospheric formaldehyde columns
25 from GOME-2/MetOp-A addressing noise reduction and instrumental degradation issues, Atmos. Meas. Tech., 5, 2933–2949, doi:10.5194/amt-5-2933-2012, 2012. 1111, 1114, 1115, 1118, 1119, 1139

Dikty, S. and Richter, A.: GOME-2 on MetOp-A: Support for Analysis of GOME-2 In-Orbit Degradation and Impacts on Level 2 Data Products, available at: http://www.iup.uni-bremen.de/
30 doas/reports/Final_Report_Level-2_Data_GOME-2_Degradation.pdf (last access: 23 January 2015), 2012. 1124

Fayt, C., De Smedt, I., Letocart, V., Merlaud, A., Pinardi, G., and Van Roozendael, M.: QDOAS software user manual, 1.00 Edn., Belgian Institute for Space Aeronomy, 2011. 1116

Title Page

Abstract | Introduction

Conclusions | References

Tables | Figures

◀ | ▶

◀ | ▶

Back | Close

Full Screen / Esc

Printer-friendly Version

Interactive Discussion

Fu, T.-M., Jacob, D. J., Palmer, P. I., Chance, K., Wang, Y. X., Barletta, B., Blake, D. R., Stanton, J. C., and Pilling, M. J.: Space-based formaldehyde measurements as constraints on volatile organic compound emissions in east and south Asia and implications for ozone, J. Geophys. Res., 112, 6312, doi:10.1029/2006JD007853, 2007. 1111, 1112, 1115, 1129

González Abad, G., Liu, X., Chance, K., Wang, H., Kurosu, T. P., and Suleiman, R.: Updated Smithsonian Astrophysical Observatory Ozone Monitoring Instrument (SAO OMI) formaldehyde retrieval, Atmos. Meas. Tech., 8, 19–32, doi:10.5194/amt-8-19-2015, 2015. 1111, 1114, 1118, 1139

Gonzi, S., Palmer, P. I., Barkley, M. P., Smedt, I. D., and Roozendael, M. V.: Biomass burning emission estimates inferred from satellite column measurements of HCHO: Sensitivity to co-emitted aerosol and injection height, Geophys. Res. Lett., 38, L14807, doi:10.1029/2011GL047890, 2011. 1115

Guenther, A., Karl, T., Harley, P., Wiedinmyer, C., Palmer, P. I., and Geron, C.: Estimates of global terrestrial isoprene emissions using MEGAN (Model of Emissions of Gases and Aerosols from Nature), Atmos. Chem. Phys., 6, 3181–3210, doi:10.5194/acp-6-3181-2006, 2006. 1117

Heckel, A., Kim, S.-W., Frost, G. J., Richter, A., Trainer, M., and Burrows, J. P.: Influence of low spatial resolution a priori data on tropospheric NO_2 satellite retrievals, Atmos. Meas. Tech., 4, 1805–1820, doi:10.5194/amt-4-1805-2011, 2011. 1115, 1120

Herman, J. R. and Celarier, E. A.: Earth surface reflectivity climatology at 340–380 nm from TOMS data, J. Geophys. Res., 102, 28003–28011, doi:10.1029/97JD02074, 1997. 1114, 1118, 1123, 1139, 1141

Hewson, W., Bösch, H., Barkley, M. P., and De Smedt, I.: Characterisation of GOME-2 formaldehyde retrieval sensitivity, Atmos. Meas. Tech., 6, 371–386, doi:10.5194/amt-6-371-2013, 2013. 1111, 1115, 1116, 1118

Kleipool, Q. L., Dobber, M. R., de Haan, J. F., and Levelt, P. F.: Earth surface reflectance climatology from 3 years of OMI data, J. Geophys. Res., 113, D18308, doi:10.1029/2008JD010290, 2008. 1114, 1115, 1123, 1127, 1139, 1140, 1141

Koelemeijer, R. B. A., de Haan, J. F., and Stammes, P.: A database of spectral surface reflectivity of the Earth in the range 335–772 nm derived from 5.5 years of GOME observations, J. Geophys. Res., 108, 4070, doi:10.1029/2002JD002429, 2003. 1114

Title Page

Abstract   Introduction

Conclusions   References

Tables   Figures

◀◀   ▶▶

◀   ▶

Back   Close

Full Screen / Esc

Printer-friendly Version

Interactive Discussion

Köpke, P., Hess, M. Schult, I., and Shettle, E. P.: Global aerosol data set, Max-Planck-Institut für Meteorologie Hamburg, Germany, available at: http://rascin.net/sites/default/files/downloads/MPI-Report_243.pdf (last access: 23 January 2015), 1997. 1118

Kurosu, T. P., Chance, K., and Sioris, C.: Preliminary results for HCHO and BrO from the EOS-Aura Ozone Monitoring Instrument, in: Passive Optical Remote Sensing of the Atmosphere and Clouds IV, Proc. of SPIE, vol. 5652, 116–123, doi:10.1117/12.578606, 2004. 1111

Lee, C., Martin, R. V., van Donkelaar, A., O'Byrne, G., Krotkov, N., Richter, A., Huey, L. G., and Holloway, J. S.: Retrieval of vertical columns of sulfur dioxide from SCIAMACHY and OMI: air mass factor algorithm development, validation, and error analysis, J. Geophys. Res., 114, D22303, doi:10.1029/2009JD012123, 2009. 1125

Lin, J.-T., Martin, R. V., Boersma, K. F., Sneep, M., Stammes, P., Spurr, R., Wang, P., Van Roozendael, M., Clémer, K., and Irie, H.: Retrieving tropospheric nitrogen dioxide from the Ozone Monitoring Instrument: effects of aerosols, surface reflectance anisotropy, and vertical profile of nitrogen dioxide, Atmos. Chem. Phys., 14, 1441–1461, doi:10.5194/acp-14-1441-2014, 2014. 1120, 1140

Loyola, D., Valks, P., Hao, N., Rix, M., and Slijkhuis, S.: Algorithm Theoretical Basis Document for GOME-2 Total Column Products of Ozone, NO2, tropospheric NO_2, BrO, SO_2, H_2O, HCHO, OClO and Cloud Properties, Tech. Rep. DLR/GOME-2/ATBD/01, EUMETSAT, 2011. 1125

Malicet, J., Daumont, D., Charbonnier, J., Parisse, C., Chakir, A., and Brion, J.: Ozone UV spectroscopy. I I. Absorption cross-sections and temperature dependence, J. Atmos. Chem., 21, 263–273 doi:10.1007/BF00696758, 1995. 1124

Mao, J., Paulot, F., Jacob, D. J., Cohen, R. C., Crounse, J. D., Wennberg, P. O., Keller, C. A., Hudman, R. C., Barkley, M. P., and Horowitz, L. W.: Ozone and organic nitrates over the eastern United States: sensitivity to isoprene chemistry, J. Geophys. Res., 118, 11256–11268, doi:10.1002/jgrd.50817, 2013. 1117

Marais, E. A., Jacob, D. J., Kurosu, T. P., Chance, K., Murphy, J. G., Reeves, C., Mills, G., Casadio, S., Millet, D. B., Barkley, M. P., Paulot, F., and Mao, J.: Isoprene emissions in Africa inferred from OMI observations of formaldehyde columns, Atmos. Chem. Phys., 12, 6219–6235, doi:10.5194/acp-12-6219-2012, 2012. 1111

Martin, R. V., Chance, K., Jacob, D. J., Kurosu, T. P., Spurr, R. J. D., Bucsela, E., Gleason, J. F., Palmer, P. I., Bey, I., Fiore, A. M., Li, Q., Yantosca, R. M., and Koelemeijer, R. B. A.: An

improved retrieval of tropospheric nitrogen dioxide from GOME, J. Geophys. Res., 107, 4437, doi:10.1029/2001JD001027, 2002. 1113, 1118

Martin, R. V., Jacob, D. J., Yantosca, R. M., Chin, M., and Ginoux, P.: Global and regional decreases in tropospheric oxidants from photochemical effects of aerosols, J. Geophys. Res., 108, 4097, doi:10.1029/2002JD002622, 2003. 1118

Meller, R. and Moortgat, G. K.: Temperature dependence of the absorption cross sections of formaldehyde between 223 and 323 K in the wavelength range 225–375 nm, J. Geophys. Res., 105, 7089–7101, doi:10.1029/1999JD901074, 2000. 1124

Millet, D. B., Jacob, D. J., Turquety, S., Hudman, R. C., Wu, S., Fried, A., Walega, J., Heikes, B. G., Blake, D. R., Singh, H. B., Anderson, B. E., and Clarke, A. D.: Formaldehyde distribution over North America: implications for satellite retrievals of formaldehyde columns and isoprene emission, J. Geophys. Res., 111, 2156–2202, doi:10.1029/2005JD006853, 2006. 1111

Millet, D. B., Jacob, D. J., Boersma, F., Fu, T.-M., Kurosu, T. P., Chance, K., Heald, C. L., and Guenther, A.: Spatial distribution of isoprene emissions from North America dervied from formaldehyde column measurements by the OMI satellite sensor, J. Geophys. Res., 113, D02307, doi:10.1029/2007JD008950, 2008. 1111

Olivier, J. G. J., Berdowski, J. J. M., Peters, J. A. H. W., Bakker, J., Visschedijk, A. J. H., and Bloos, J. P. J.: Applications of EDGAR. Including a description of EDGAR 3.2: reference database with trend data for 1970–1995, RIVM, Bilthoven, RIVM report 773301 001/NRP report 410200 051, 2001. 1117

Palmer, P. I., Jacob, D. J., Chance, K., Martin, R. V., Spurr, R. J. D., Kurosu, T. P., Bey, I., Yantosca, R., Fiore, A., and Li, Q.: Air mass factor formulation for spectroscopic measurements from satellites: application to formaldehyde retrievals from the Global Ozone Monitoring Experiment, J. Geophys. Res., 106, 14539–14550, doi:10.1029/2000JD900772, 2001. 1112, 1113, 1114, 1118

Palmer, P. I., Abbot, D. S., Fu, T.-M., Jacob, D. J., Chance, K., Kurosu, T., Guenther, A., Wiedinmyer, C., Stanton, J., Pilling, M., Pressley, S., Lamb, B., and Sumner, A. L.: Quantifying the seasonal and interannual variability of North American isoprene emissions using satellite observations of formaldehyde column, J. Geophys. Res., D12315, doi:10.1029/2005JD006689, 2006. 1111, 1112, 1128

GOME-2 airmass factors

W. Hewson et al.

Title Page

Abstract | Introduction

Conclusions | References

Tables | Figures

◄ | ►

◄ | ►

Back | Close

Full Screen / Esc

Printer-friendly Version

Interactive Discussion

Paulot, F., Crounse, J. D., Kjaergaard, H. G., Kroll, J. H., Seinfeld, J. H., and Wennberg, P. O.: Isoprene photooxidation: new insights into the production of acids and organic nitrates, Atmos. Chem. Phys., 9, 1479–1501, doi:10.5194/acp-9-1479-2009, 2009a. 1117

Paulot, F., Crounse, J. D., Kjaergaard, H. G., Kurten, A., St. Clair, J. M., Seinfeld, J. H., and Wennberg, P. O.: Unexpected epoxide formation in the gas-phase photooxidation of isoprene, Science, 325, 730–733, doi:10.1126/science.1172910, 2009b. 1117

Platt, U. and Stutz, J.: Differential Optical Absorption Spectroscopy, Physics of Earth and Space Environments, Springer, Berlin, 2008. 1116

Popp, C., Wang, P., Brunner, D., Stammes, P., Zhou, Y., and Grzegorski, M.: MERIS albedo climatology for FRESCO+ O_2 A-band cloud retrieval, Atmos. Meas. Tech., 4, 463–483, doi:10.5194/amt-4-463-2011, 2011. 1114, 1118

Rienecker, M., Suarez, M. R., Todling, J. B., Takacs, L., Liu, H.-C., Gu, W., Sienkiewicz, M., Koster, R., Gelaro, R., Stajner, I., and Nielsen, J.: The GEOS-5 Data Assimilation System – Documentation of Versions 5.0.1, 5.1.0, and 5.2.0, Technical Report Series on Global Modeling and Data Assimilation, NASA Global Modeling and Assimilation Office, available at: http://gmao.gsfc.nasa.gov/pubs/tm/docs/Rienecker369.pdf (last access: 23 January 2015), 2008. 1117

Rozanov, A., Rozanov, V., Buchwitz, M., Kokhanovsky, A., and Burrows, J. P.: SCIATRAN 2.0 – A new radiative transfer model for geophysical applications in the 175–2400 nm spectral region, Adv. Space Res., 36, 1015–1019, doi:10.1016/j.asr.2005.03.012, 2005. 1125

Russell, A. R., Perring, A. E., Valin, L. C., Bucsela, E. J., Browne, E. C., Wooldridge, P. J., and Cohen, R. C.: A high spatial resolution retrieval of NO_2 column densities from OMI: method and evaluation, Atmos. Chem. Phys., 11, 8543–8554, doi:10.5194/acp-11-8543-2011, 2011. 1114, 1115, 1120, 1140

Schaub, D., Brunner, D., Boersma, K. F., Keller, J., Folini, D., Buchmann, B., Berresheim, H., and Staehelin, J.: SCIAMACHY tropospheric NO_2 over Switzerland: estimates of NO_x lifetimes and impact of the complex Alpine topography on the retrieval, Atmos. Chem. Phys., 7, 5971–5987, doi:10.5194/acp-7-5971-2007, 2007. 1115

Spurr, R. J. D.: A Simultaneous radiative transfer derivation of intensities and weighting functions in a general pseudo-spherical treatment, J. Quant. Spectrosc. Ra., 75, 129–175, 2002. 1118

Spurr, R.: Area-weighting tessellation for nadir-viewing spectrometers, Internal Technical Note, Harvard-Smithsonian Centre for Astrophysics, 2003. 1121

GOME-2 airmass factors

W. Hewson et al.

Title Page

Abstract	Introduction
Conclusions	References
Tables	Figures

|◄ | ►|

◄ | ►

Back | Close

Full Screen / Esc

Printer-friendly Version

Interactive Discussion

Stavrakou, T., Müller, J.-F., De Smedt, I., Van Roozendael, M., van der Werf, G. R., Giglio, L., and Guenther, A.: Evaluating the performance of pyrogenic and biogenic emission inventories against one decade of space-based formaldehyde columns, Atmos. Chem. Phys., 9, 1037–1060, doi:10.5194/acp-9-1037-2009, 2009a. 1110

Stavrakou, T., Müller, J.-F., De Smedt, I., Van Roozendael, M., van der Werf, G. R., Giglio, L., and Guenther, A.: Global emissions of non-methane hydrocarbons deduced from SCIA-MACHY formaldehyde columns through 2003–2006, Atmos. Chem. Phys., 9, 3663–3679, doi:10.5194/acp-9-3663-2009, 2009b. 1111

Stavrakou, T., Müller, J.-F., Bauwens, M., De Smedt, I., Van Roozendael, M., Guenther, A., Wild, M., and Xia, X.: Isoprene emissions over Asia 1979–2012: impact of climate and land-use changes, Atmos. Chem. Phys., 14, 4587–4605, doi:10.5194/acp-14-4587-2014, 2014. 1111

Valks, P., Pinardi, G., Richter, A., Lambert, J.-C., Hao, N., Loyola, D., Van Roozendael, M., and Emmadi, S.: Operational total and tropospheric NO_2 column retrieval for GOME-2, Atmos. Meas. Tech., 4, 1491–1514, doi:10.5194/amt-4-1491-2011, 2011. 1115, 1116, 1140

van der Werf, G. R., Randerson, J. T., Giglio, L., Collatz, G. J., Kasibhatla, P. S., and Arellano Jr., A. F.: Interannual variability in global biomass burning emissions from 1997 to 2004, Atmos. Chem. Phys., 6, 3423–3441, doi:10.5194/acp-6-3423-2006, 2006. 1117

van Donkelaar, A., Martin, R. V., Leaitch, W. R., Macdonald, A. M., Walker, T. W., Streets, D. G., Zhang, Q., Dunlea, E. J., Jimenez, J. L., Dibb, J. E., Huey, L. G., Weber, R., and Andreae, M. O.: Analysis of aircraft and satellite measurements from the Intercontinental Chemical Transport Experiment (INTEX-B) to quantify long-range transport of East Asian sulfur to Canada, Atmos. Chem. Phys., 8, 2999–3014, doi:10.5194/acp-8-2999-2008, 2008. 1117

Wang, P., Stammes, P., van der A, R., Pinardi, G., and van Roozendael, M.: FRESCO+: an improved O_2 A-band cloud retrieval algorithm for tropospheric trace gas retrievals, Atmos. Chem. Phys., 8, 6565–6576, doi:10.5194/acp-8-6565-2008, 2008. 1118, 1127

Wittrock, F., Richter, A., Ladstätter-Weißenmayer, A., and Burrows, J. P.: Global observations of formaldehyde, in: European Space Agency, (Special Publication) ESA SP, 1358–1362, 2000. 1111

Wittrock, F., Richter, A., Oetjen, H., Burrows, J. P., Kanakidou, M., Myriokefalitakis, S., Volkamer, R., Beirle, S., Platt, U., and Wagner, T.:Simultaneous global observations of glyoxal and formaldehyde from space, Geophys. Res. Lett., 33, 16, doi:10.1029/2006GL026310, 2006. 1111

GOME-2 airmass factors

W. Hewson et al.

Title Page

Abstract | Introduction

Conclusions | References

Tables | Figures

◄◄ | ►►

◄ | ►

Back | Close

Full Screen / Esc

Printer-friendly Version

Interactive Discussion

Zhou, Y., Brunner, D., Boersma, K. F., Dirksen, R., and Wang, P.: An improved tropospheric NO_2 retrieval for OMI observations in the vicinity of mountainous terrain, Atmos. Meas. Tech., 2, 401–416, doi:10.5194/amt-2-401-2009, 2009. 1115, 1119, 1121, 1122, 1146

Zhou, Y., Brunner, D., Spurr, R. J. D., Boersma, K. F., Sneep, M., Popp, C., and Buchmann, B.: Accounting for surface reflectance anisotropy in satellite retrievals of tropospheric NO_2, Atmos. Meas. Tech., 3, 1185–1203, doi:10.5194/amt-3-1185-2010, 2010. 1114, 1123

Table 1. Comparison of three different contemporary HCHO AMF calculations. Readers are referred to cited references for full details.

	Barkley et al. (2013)	De Smedt et al. (2012)	González Abad et al. (2014)
Instrument(s)	SCIAMACHY and OMI	GOME, SCIAMACHY and GOME-2	OMI
RTM	LIDORT v2.3	LIDORT v3.0	VLIDORT v2.4
CTM	GEOS-Chem Nested $0.67° \times 0.5°$ grid	IMAGES v2 Global $2° \times 2.5°$ grid	GEOS-Chem Global $2° \times 2.5°$ grid
A Priori Profile	GEOS-Chem monthly mean profiles	IMAGESv2 daily profiles	GEOS-Chem monthly mean profiles
Surface Pressure	GEOS-Chem $(0.67° \times 0.5°)$	IMAGESv2 $(2° \times 2.5°)$ adjusted by mean elevation	GEOS-Chem $(2° \times 2.5°)$
Surface Elevation	–	not specified	–
Surface Albedo	Herman and Celarier (1997) monthly climatology regridded to $0.67° \times 0.5°$ $(\lambda \sim 360 \, nm)$	Kleipool et al. (2008) monthly climatology at $0.5° \times 0.5°$ $(\lambda = 342 \, nm)$	Kleipool et al. (2008) monthly climatology at $0.5° \times 0.5°$ (interpolated to $\lambda \sim 340 \, nm$)
Aerosol Correction	GEOS-Chem monthly mean AOD profiles	Implicit treatment using cloud algorithm	Implicit treatment using cloud algorithm
Pixel Calculation	Interpolated from look-up table	Interpolated from look-up table	Interpolated from look-up table

Discussion Paper | Discussion Paper | Discussion Paper | Discussion Paper |

AMTD

8, 1109–1150, 2015

GOME-2 airmass factors

W. Hewson et al.

Title Page

Abstract | Introduction

Conclusions | References

Tables | Figures

◄◄ | ►►

◄ | ►

Back | Close

Full Screen / Esc

Printer-friendly Version

Interactive Discussion

Table 2. Comparison of four different contemporary NO_2 AMF calculations. Readers are referred to cited references for full details.

	Boersma et al. (2011a)	Lin et al. (2014)	Russell et al. (2011)	Valks et al. (2011)
Instrument(s)	OMI	OMI	OMI	GOME-2
RTM	KNMI DAK	LIDORT v3.6	TOMRAD	LIDORT v3.3
CTM	TM4 Global 2° × 3° grid	GEOS-Chem Nested 0.5° × 0.67° grid	WRF-Chem Regional 4 km × 4 km grid	MOZART v2 Global 1.85° × 1.85° grid
A Priori Profile	TM4 daily profiles	GEOS-CHEM daily profiles	WRF-Chem monthly mean profiles	MOZART monthly mean profiles
Surface Pressure	TM4 (2° × 3°) adjusted by mean elevation	GEOS-Chem (0.67° × 0.5°) adjusted by mean elevation	WRF-Chem (4 km × 4 km grid) adjusted by mean elevation	MOZART (1.85° × 1.85°) adjusted by mean elevation
Surface Elevation	DEM-3 km	GMTED2010	GLOBE 1 km × 1 km	GOTOPO30 1 km × 1 km
Surface Albedo	Kleipool et al. (2008) monthly climatology at 0.5° × 0.5° (λ = 479.5 nm) Temporal interpolation only	MODIS MCD43C2 BDRF 16-day average at 0.05° × 0.05° (λ = 440 nm) Temporal interpolation only	MODIS MCD43C2 BDRF 16-day average at 0.05° × 0.05° (λ = 342 nm) Area-weighted	Boersma et al. (2004) monthly climatology at 1° × 1.25° (λ = 380 and 440 nm) Area-weighted and temporal interpolation
Aerosol Correction	Implicit treatment using cloud algorithm	GEOS-Chem daily AOD profiles (AOD_λ = 438 nm) Adjusted by AERONET, MAX-DOAS and MODIS	Implicit treatment using cloud algorithm	Implicit treatment using cloud algorithm
Pixel Calculation	Interpolated from look-up table	RTM calculation for each scene	Interpolated from look-up table	Interpolated from look-up table

Table 3. Summary of the baseline and updated UoL AMF algorithm.

	Baseline AMF algorithm	Updated AMF algorithm
CTM	GEOS-Chem global 4° × 5° grid	GEOS-Chem global 2° × 2.5° grid
A Priori Profile	GEOS-Chem daily profiles – selected using observation centre coordinates	GEOS-Chem daily profiles – area-weighted mean for observation footprint
Surface Pressure	GEOS-Chem (4° × 5°)	GEOS-Chem (2° × 2.5°) – adjusted by area-weighted mean elevation
Surface Albedo	Herman and Celarier (1997) monthly climatology – regridded to 4° × 5° ($\lambda \sim 360$ nm)	Kleipool et al. (2008) monthly climatology – default 0.5° × 0.5° ($\lambda = 342$ nm) – area-weighted and time interpolated
Surface Elevation	n/a	GMTED2010 (0.0083° × 0.0083°)
LIDORT cross-sections	Fixed OMI cross section	Orbit specific GOME-2
LIDORT O_3 profile	US Standard atmosphere	Monthly and latitudinal TOMS v8 climatology – scaled to coincident GOME-2 total ozone observations
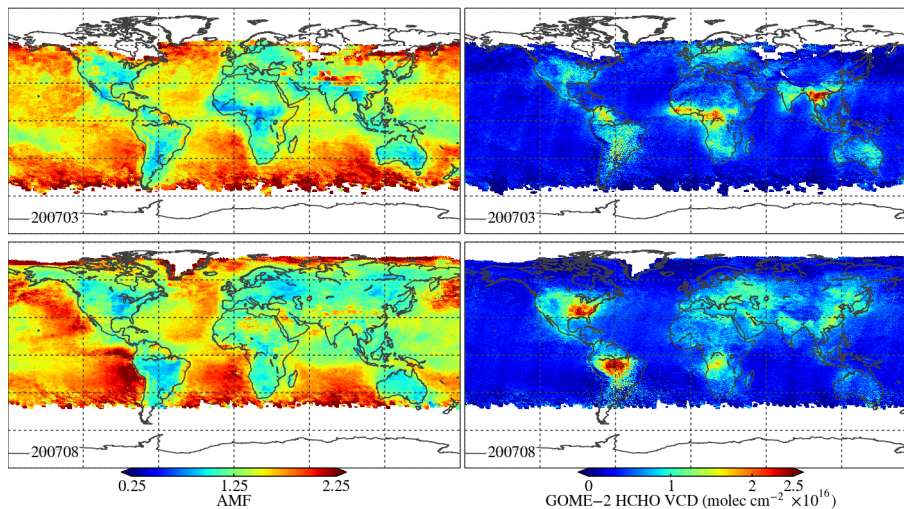
Figure 1. Monthly mean GOME-2 HCHO airmass factors (AMF) and corresponding vertical columns (VCD) for March and August 2007, calculated using the UoL baseline AMF algorithm (see Sect. 4.3) and gridded to 0.25° × 0.25° using observations with cloud fractions < 40 %.
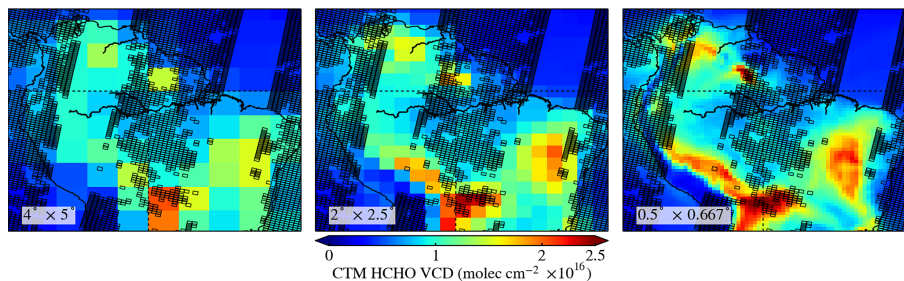
Figure 2. Model HCHO vertical columns over the Amazon simulated by GEOS-Chem at three different spatial resolutions (left to right: $4° × 5°$, $2° × 2.5°$, $0.5° × 0.667°$). Overlain in black are three typical orbital tracks showing the footprint of each GOME-2 observation with cloud fraction $< 40\%$.
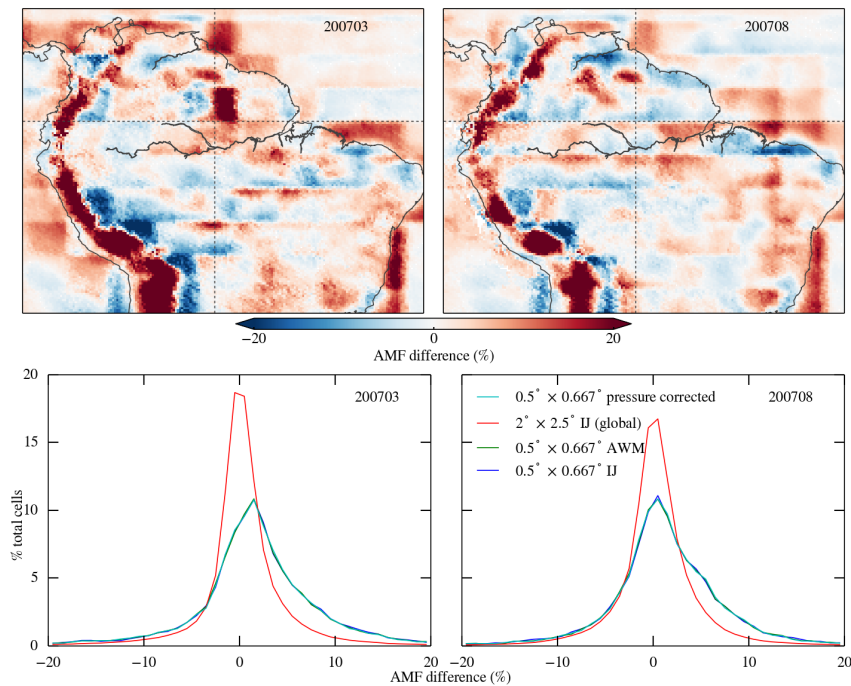
Figure 3. Top row: spatial maps of monthly mean AMF differences for March and August 2007, relative to the default UoL AMF algorithm, resulting from the use of atmospheric profiles from the GEOS-Chem 0.5° × 0.67° nested-grid simulation, as outlined in Sect. 5.2. The AMFs are gridded on to 0.25° × 0.25° using observations with cloud fractions < 40 %. Bottom row: the corresponding histograms of the AMF differences for these two months are shown in blue. The histogram of global AMF differences arising from use of atmospheric profiles from GEOS-Chem's 2° × 2.5° simulation is shown in red. Also shown, are histograms resulting from the area-weighting (green) and surface pressure corrected (aqua) of the 0.5° × 0.67° nested-grid profiles, as discussed in Sects. 5.3 and 5.4 respectively. Note closeness of lines detailing derivatives of the high resolution 0.5° × 0.67° grids.
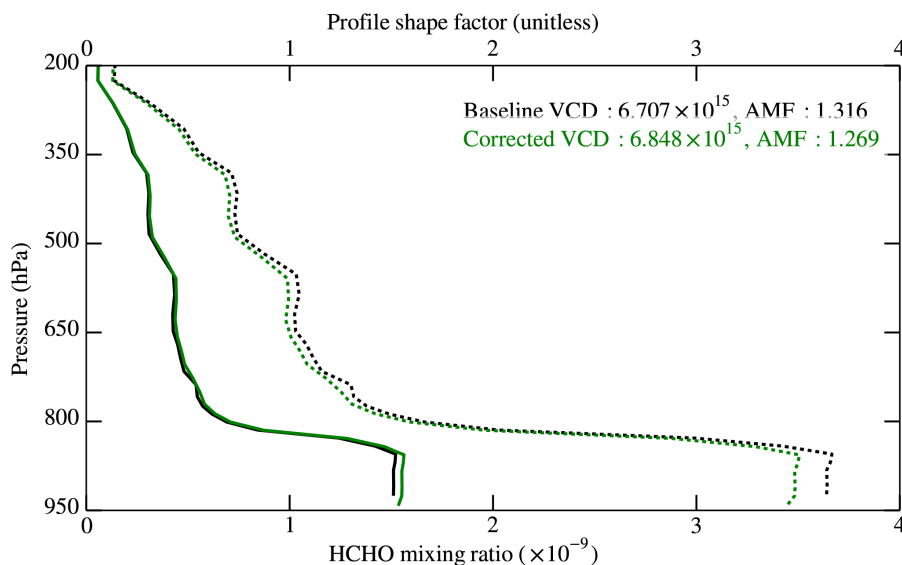
Figure 4. Effect of the vertical profile pressure correction (Sect. 5.4 of main text) for a scan over the Ecuadorian Andes (78° W 1° N); with HCHO mixing ratios (solid line) along the bottom *x* axis and corresponding calculated shape factor *S* (dotted line) on the top axis. The corrected model HCHO profile is shifted upwards and reduced in magnitude as a result of the lower surface pressure value on which to base the profile. Scattering weights are accordingly reduced, acting to reduce the AMF for this scan, and subsequently increase the calculated HCHO VCD.
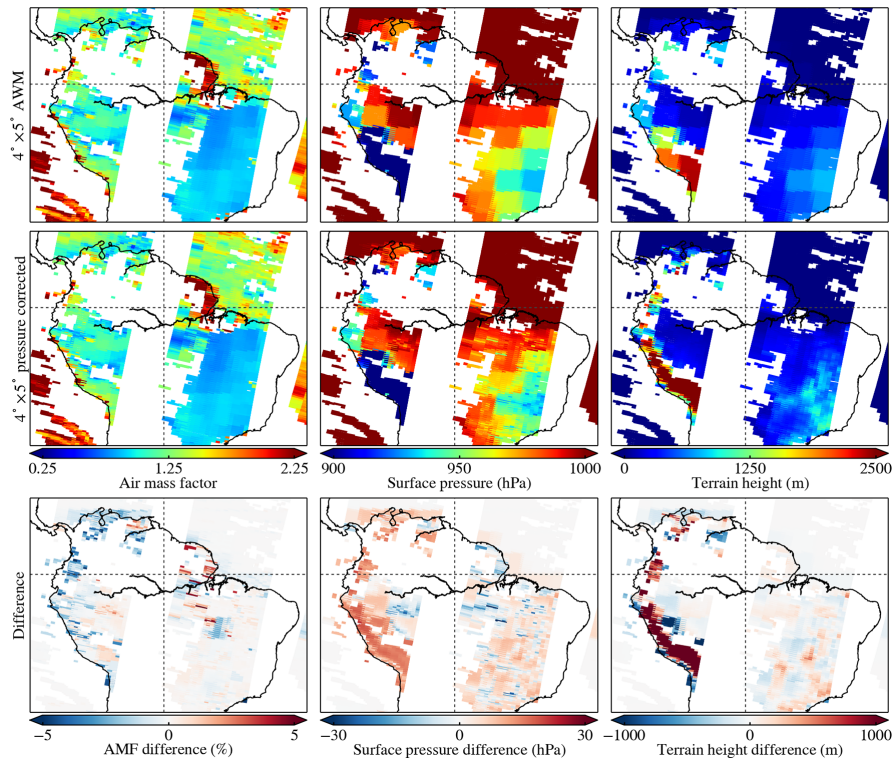
Figure 5. GOME-2 orbital tracks over the Amazon showing the effect of the Zhou et al. (2009) pressure correction (Sect. 5.4) against a fully area weighted set of GEOS-Chem 4° × 5° inputs (Sect. 5.3). Left to right the first two rows (area weighted mean only inputs, and pressure corrected AWM inputs on the second) show AMF, model surface pressure and terrain height; whilst the bottom row details difference between these parameters for both cases. In this case, differences between the two tests are exclusively due to the pressure correction alone. As such, the correction is most noticeable over mountainous terrain, causing AMF differences of about ±5 %.
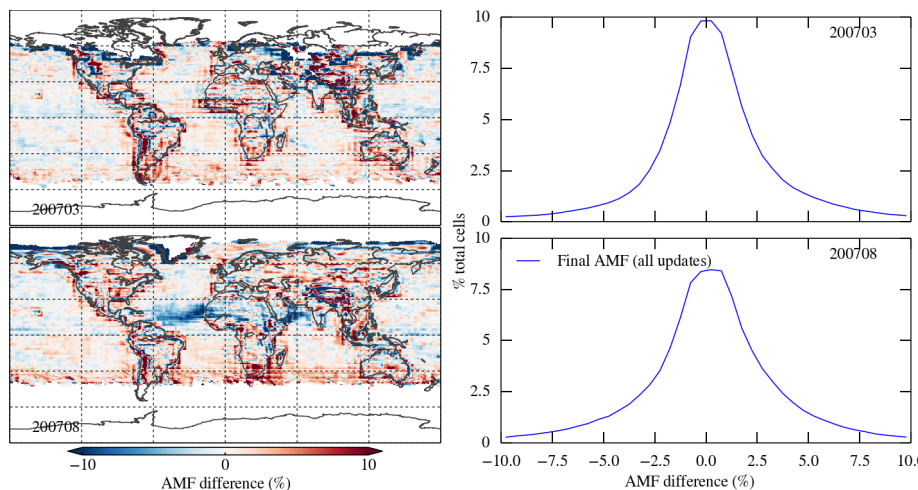
Figure 6. Left: spatial maps of monthly mean AMF differences for March and August 2007 between the initial UoL IJ AMF calculation, and the final per-pixel AMF with all algorithm updates included, as discussed in Sect. 5.8. The AMFs are gridded to a $0.25° \times 0.25°$ using observations with cloud fractions $< 40\%$. Right: corresponding histograms of the AMF differences are shown in blue.

Total AMF error (%)

0   37.5   75
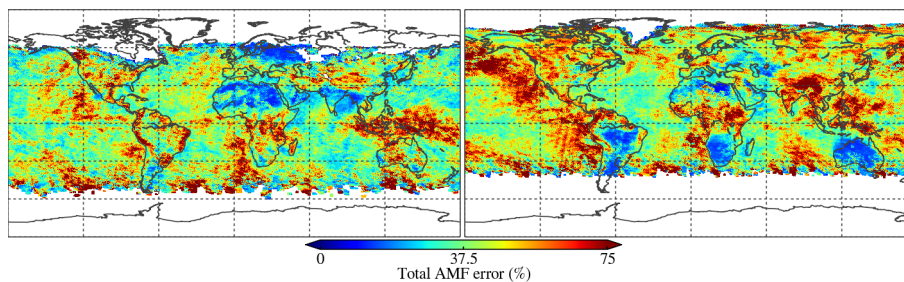
Figure 7. Monthly mean GOME-2 total AMF errors for March (left) and August (right) 2007 calculated using Eq. (6). The AMF errors are gridded to a 0.25° × 0.25° grid using observations with cloud fractions < 40 %.
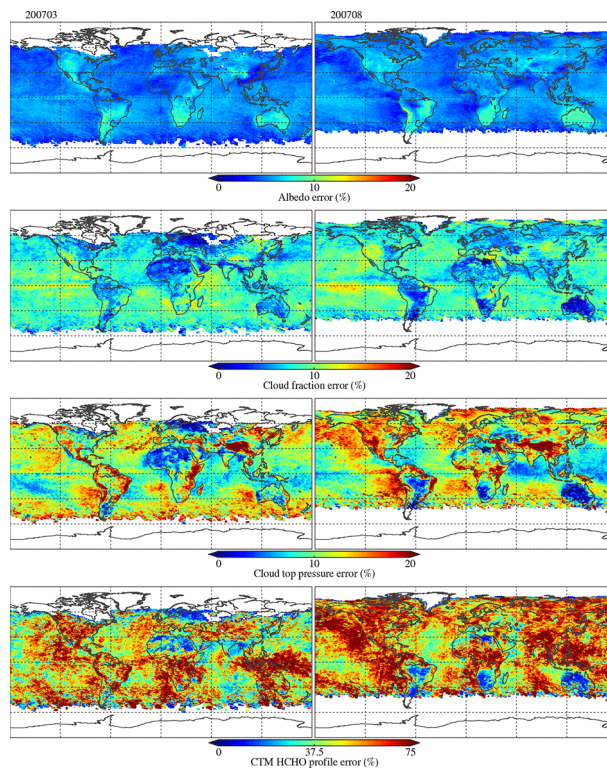
Figure 8. Monthly mean GOME-2 component albedo, cloud fraction, cloud top pressure and CTM HCHO profile AMF errors for March (left) and August (right) 2007. Errors are gridded to a 0.25° × 0.25° grid using observations with cloud fractions < 40 %.
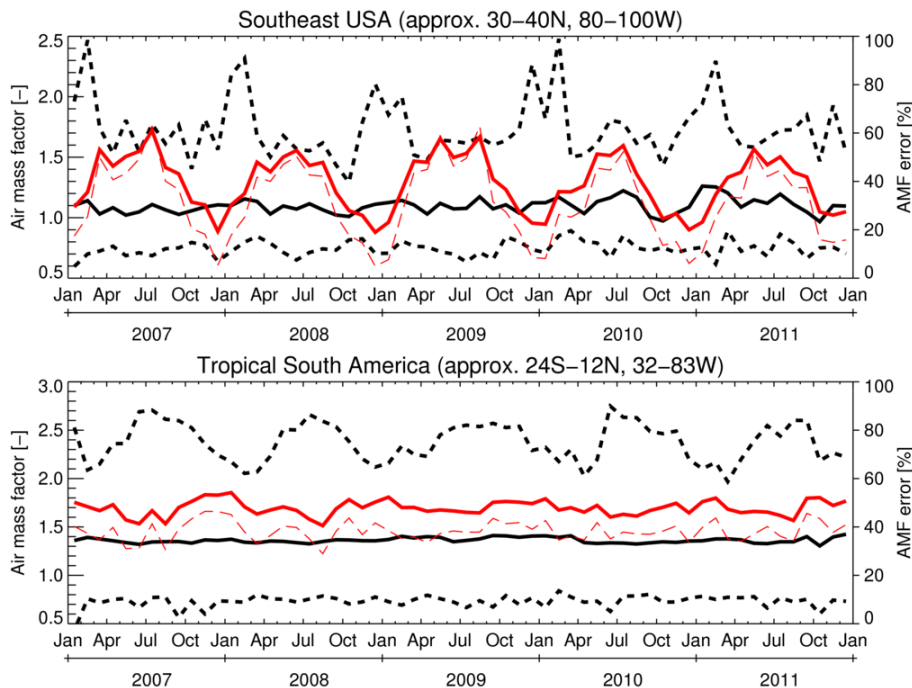
Figure 9. 2007–2011 time series over southeast USA (top) and tropical South America (bottom), showing the monthly maximum, minimum and mean AMFs (dashed and solid black lines, respectively), and the total AMF error (red solid line). The dashed red line shows the contribution to the total AMF error from uncertainty in the HCHO profile shape.